

# SMA OBSERVATIONS ON FAINT SUBMILLIMETER GALAXIES WITH $S_{850} < 2$ mJy: ULTRA DUSTY LOW-LUMINOSITY GALAXIES AT HIGH REDSHIFT

CHIAN-CHOU CHEN<sup>1,2</sup>, LENNOX L. COWIE<sup>1</sup>, AMY J. BARGER<sup>1,3,4</sup>, WEI-HAO WANG<sup>5</sup>, JONATHAN P. WILLIAMS<sup>1</sup>

*Accepted to The Astrophysical Journal*

## ABSTRACT

We obtained SMA observations of eight faint (intrinsic 850  $\mu\text{m}$  fluxes  $< 2$  mJy) submillimeter galaxies (SMGs) discovered in SCUBA images of the massive lensing cluster fields A370, A2390, and A1689 and detected five. In total, we obtain 5 SMA detections, all of which have de-lensed fluxes  $< 1$  mJy with estimated total infrared luminosities  $10^{10} - 10^{12} L_{\odot}$ , comparable to luminous infrared galaxies (LIRGs) and normal star-forming galaxies. Based on the latest number counts, these galaxies contribute  $\sim 70\%$  of the 850  $\mu\text{m}$  extragalactic background light and represent the dominant star-forming galaxy population in the dusty universe. However, only  $40^{+30}_{-16}\%$  of our faint SMGs would be detected in deep optical or near-infrared surveys, which suggests many of these sources are at high redshifts ( $z \gtrsim 3$ ) or extremely dusty, and they are not included in current star formation history estimates.

*Subject headings:* cosmology: observations — galaxies: formation — galaxies: starburst — gravitational lensing: strong — submillimeter: galaxies

## 1. INTRODUCTION

Bright submillimeter galaxies (SMGs;  $S_{850\mu\text{m}} > 2$  mJy) have luminosities corresponding to those of local ultraluminous infrared galaxies (ULIRGs;  $L_{\text{IR}} > 10^{12} L_{\odot}$ ). Many of these sources have very faint optical or near-infrared counterparts, reflecting their large dust contents and high redshifts (e.g., Younger et al. 2009; Barger et al. 2012; Walter et al. 2012; Simpson et al. 2014). However, as we move to lower submillimeter fluxes, we might expect the SMG population to become less dusty, because the spectral energy distributions become more UV dominated for lower infrared luminosities (e.g., Chary & Elbaz 2001), and hence for the faint SMG population to be substantially overlapped with the optically selected population. The goal of the present paper is to test this expectation, given how critical it is to obtain an accurate determination of the star formation history.

Many blank-field 850  $\mu\text{m}$  surveys have been made with ground-based, single-dish telescopes, such as the James Clerk Maxwell Telescope (JCMT) and the Atacama Pathfinder Experiment (APEX) (Barger et al. 1998; Hughes et al. 1998; Eales et al. 1999, 2000; Scott et al. 2002; Smail et al. 2002; Borys et al. 2003; Serjeant et al. 2003; Webb et al. 2003; Wang et al. 2004; Coppin et al. 2006; Weiß et al. 2009; Casey et al. 2013; Geach et al. 2013; Barger et al. 2014). Detailed follow-up continuum and emission line studies have shown that many of these SMGs (review by Blain et al. 2002) are at high redshifts with  $2 < z < 5$  (e.g., Chapman et al. 2005;

Wardlow et al. 2011; Walter et al. 2012; Barger et al. 2012), gas rich ( $M_{\text{gas}} > 10^{10} M_{\odot}$ ; e.g., Greve et al. 2005; Bothwell et al. 2013), highly clustered (e.g., Scott et al. 2006; Hickox et al. 2012), have both disk-like and merger-like morphologies (e.g., Tacconi et al. 2008; Hodge et al. 2012), and may be the progenitors of massive elliptical galaxies (e.g., Lilly et al. 1999; Fu et al. 2013; Simpson et al. 2014). Using stellar population synthesis models, the derived stellar masses of SMGs are typically in the range  $\sim 10^{11} - 10^{12} M_{\odot}$  (e.g., Borys et al. 2005; Dye et al. 2008; Michałowski et al. 2012). Incorporating the shorter wavelength data from the *Herschel Space Observatory* (hereafter, *Herschel*), Magnelli et al. (2012) argued that 850  $\mu\text{m}$  selected SMGs are diverse in dust temperature (20–60 K). However, Barger et al. (2014) using a small, uniformly selected sample of 850  $\mu\text{m}$  sources lying in the flux range 3–15 mJy, found a much smaller range of temperatures. X-ray observations of 850  $\mu\text{m}$  selected SMGs with radio and/or mid-infrared (MIR) counterparts have revealed, on average, order of magnitude lower X-ray-to-far-infrared (FIR) luminosity ratios for SMGs than for AGN dominated quasars, and FIR luminosity outputs dominated by star formation (e.g., Alexander et al. 2005; Laird et al. 2010; Symeonidis et al. 2011; Wang et al. 2013). Despite their rareness, the extreme star formation rates ( $\text{SFR} \sim 500 - 10000 M_{\odot} \text{ yr}^{-1}$ ) of SMGs make them substantial contributors to star formation in the early universe (e.g., Barger et al. 2000, 2012, 2014; Chapman et al. 2005; Wang et al. 2006; Serjeant et al. 2008; Wardlow et al. 2011; Casey et al. 2013; Swinbank et al. 2014).

However, the blank-field SMGs only contribute 20 – 30% of the 850  $\mu\text{m}$  extragalactic background light (EBL; e.g., Barger et al. 1999; Coppin et al. 2006; Chen et al. 2013a,b), which is the integrated emission from all extragalactic sources along the line-of-sight. Thus, the bulk of dusty star formation is still unresolved, and determining the characteristics of the faint SMGs with typical  $L_{\text{IR}} < 10^{12} L_{\odot}$  that emit most of the 850  $\mu\text{m}$  EBL is needed for a full understanding of the cosmic star forma-

<sup>1</sup> Institute for Astronomy, University of Hawaii, 2680 Woodlawn Drive, Honolulu, HI 96822.

<sup>2</sup> Institute for Computational Cosmology, Department of Physics, Durham University, South Road, Durham DH1 3LE, UK

<sup>3</sup> Department of Astronomy, University of Wisconsin-Madison, 475 North Charter Street, Madison, WI 53706.

<sup>4</sup> Department of Physics and Astronomy, University of Hawaii, 2505 Correa Road, Honolulu, HI 96822.

<sup>5</sup> Academia Sinica Institute of Astronomy and Astrophysics, P.O. Box 23-141, Taipei 10617, Taiwan.

TABLE 1  
SMA OBSERVATIONS

I.D.	Source Name	Track Dates	Beam <sup>c</sup> FWHM ("×")	Beam <sup>c</sup> P.A. (deg)	$\sigma^c$ (mJy/ beam)	Flux Calibrator(s)	Passband Calibrator(s)	Gain Calibrator(s)
(1)	(2)	(3)	(4)	(5)	(6)	(7)	(8)	(9)
Chen-1	#4 <sup>a</sup>	20121030, 20121109, 20121111	2.08×2.06	55.8	0.61	Neptune	billac	0309+104, 0339-017
Chen-2	#12 <sup>a,g</sup>	20090626 <sup>d</sup> , 20090627 <sup>d</sup> , 20091016	1.98×1.63	44.8	0.80	Callisto, Uranus	3c454.3	3c454.3, 2148+069
Chen-3	#14 <sup>a</sup>	20110524, 20110925	2.22×1.80	-33.3	1.01	Uranus	3c454.3, 3c84	3c454.3, 2203+174
Chen-4	SMM J131128.6-012036 <sup>b</sup>	20120506, 20120509	1.93×1.74	80.7	0.92	Neptune, Titan	billac, 3c279	3c279, 3c273, 1337-129
Chen-5	SMM J131129.1-012049 <sup>b</sup>	20120508	2.05×1.78	78.6	1.10	Titan	billac	3c273, 1337-129
Chen-6	SMM J131132.0-011955 <sup>b</sup>	20130226, 20130303	2.36×1.86	-43.7	0.74	Titan, Callisto	billac, 3c84	3c273, 1337-129
Chen-7	SMM J131134.1-012021 <sup>b,e</sup>	20130226, 20130303, 20130306	2.36×1.98	-43.4	0.65	Titan, Callisto	billac, 3c84	3c273, 1337-129
Chen-8	SMM J131135.1-012018 <sup>b,e</sup>	20130226, 20130303, 20130306	2.36×1.98	-43.4	1.00 <sup>f</sup>	Titan, Callisto	billac, 3c84	3c273, 1337-129

<sup>a</sup> Sources first identified by Cowie et al. (2002) with SCUBA.

<sup>b</sup> Sources first identified by Knudsen et al. (2008) with SCUBA.

<sup>c</sup> Results from all the tracks combined on a given source. The values of  $\sigma_T$  are the theoretical sensitivities, while the values of  $\sigma$  are the r.m.s. of the dirty maps.

<sup>d</sup> The bandwidth per each sideband was 2 GHz on these tracks, whereas it was 4 GHz for the others.

<sup>e</sup> Both Chen-7 and Chen-8 were observed in the same dataset. The field of view of the SMA primary beam covers these two sources.

<sup>f</sup> The sensitivity at the SCUBA position shown in Table 3.

<sup>g</sup> This source was named A2390-3 in Chen et al. (2011).

tion history.

Unfortunately, the poor resolution at 850  $\mu\text{m}$  (e.g.,  $\sim 14''$  FWHM on the 15 m JCMT) prevents us from directly measuring the faint SMGs below the 2 mJy confusion limit in blank fields. Almost all of our knowledge about faint SMGs comes from ground-based observations with single-dish telescopes in the fields of massive lensing clusters (e.g., Smail et al. 1997; Cowie et al. 2002; Kneib et al. 2004; Knudsen et al. 2009, 2010; Boone et al. 2013; Chen et al. 2013a). Due to the presence of the intervening cluster mass, the intrinsically faint fluxes of background sources are gravitationally amplified to a detectable level, and the confusion limit is reduced by the expansion of the source plane. Faint SMGs with fluxes between 0.1 and 2 mJy have been detected in this way. Although the number of faint SMGs that have been discovered in lensing fields is small compared to the number of bright SMGs that have been found in blank fields, their number density indicates that they contribute  $\sim 70\%$  of the 850  $\mu\text{m}$  EBL (Blain et al. 1999; Cowie et al. 2002; Knudsen et al. 2008; Zemcov et al. 2010; Chen et al. 2013a,b).

While many faint SMGs will eventually be observed with extremely sensitive submillimeter interferometric arrays, such as the Atacama Large Millimeter/submillimeter Array (ALMA), we can already begin to investigate some fundamental questions about faint SMGs using sources discovered in lensing fields. For example, using high spatial resolution submillimeter continuum observations with the Submillimeter Array (SMA), we can pin down the exact location of faint SMGs discovered with the SCUBA instrument on the JCMT (Holland et al. 1999) and find their true counterparts, if any, at other wavelengths. Once we know the correct counterparts, then we can study the properties of the faint SMGs, such as their colors and redshift distribution. Perhaps even more exciting, we can estimate the fraction of faint SMGs that are completely hidden from current optical/near-infrared (NIR) observations.

In this paper, we use SMA observations of an unbiased sample of eight highly amplified and intrinsically faint SCUBA-detected SMGs discovered in the fields of three massive lensing clusters, Abell 370 (A370), Abell 2390 (A2390), and Abell 1689 (A1689), to study the faint SMG population. The SCUBA sources are taken from

the catalogs of Cowie et al. (2002) and Knudsen et al. (2008). While previous studies focused on a few individual sources that had optical/NIR counterparts (e.g., Kneib et al. 2004; Knudsen et al. 2010), our only specifications are discovery in single-dish surveys and high amplifications ( $> 3$ ), meaning intrinsic 850  $\mu\text{m}$  fluxes expected to be less than 2 mJy.

In Chen et al. (2011), we already presented the SMA observations of one of the SCUBA sources in our sample, Chen-2. There we showed that despite the identification of likely candidate counterparts using a traditional  $p$ -value analysis, once we had the accurate source position from the SMA, we could see that there were no viable counterparts from the optical to the radio. The lack of a deep radio counterpart led us to conclude that Chen-2 could be at a very high redshift ( $z > 4$ ). This surprising result suggests that, while the NIR stacking analyses show that a large percentage ( $\sim 50\%$ ) of the 850  $\mu\text{m}$  EBL could come from sources at  $z < 1.5$  (Wang et al. 2006; Serjeant et al. 2008), a number of faint SMGs ( $< 2$  mJy) may lie at high redshifts, and they are likely missed by current optical/NIR observations. However, this suggestion is based on one source, and the results may not be representative of our selected sample as a whole. In this paper, we report on the full results of our analysis.

We describe the SMA data and data reduction in Section 2. We give our results in Section 3. In Section 4, we discuss the implications of our results, and in Section 5, we summarize the paper. We assume the Wilkinson Microwave Anisotropy Probe cosmology throughout:  $H_0 = 70.5 \text{ km s}^{-1} \text{ Mpc}^{-1}$ ,  $\Omega_M = 0.27$ , and  $\Omega_\Lambda = 0.73$  (Larson et al. 2011).

## 2. OBSERVATIONS AND DATA REDUCTION

### 2.1. SMA Observations

We conducted SMA<sup>6</sup> (Ho et al. 2004) observations in compact configuration (16–77 m baselines) of a sample of 8 highly-amplified SCUBA sources in the massive lensing cluster fields A370, A2390, and A1689. We expected

<sup>6</sup> The Submillimeter Array is a joint project between the Smithsonian Astrophysical Observatory and the Academia Sinica Institute of Astronomy and Astrophysics and is funded by the Smithsonian Institution and the Academia Sinica.

TABLE 2  
SPITZER SUPER MOSAICS

Field	3.6 $\mu\text{m}$ (ks)	Sensitivity ( $\mu\text{Jy}$ )	4.5 $\mu\text{m}$ (ks)	Sensitivity ( $\mu\text{Jy}$ )	5.8 $\mu\text{m}$ (ks)	Sensitivity ( $\mu\text{Jy}$ )	8.0 $\mu\text{m}$ (ks)	Sensitivity ( $\mu\text{Jy}$ )	24 $\mu\text{m}$ (ks)	Sensitivity ( $\mu\text{Jy}$ )
A370	13.0	0.3	12.3	0.3	13.1	1.5	11.8	1.5	2.6	31
A2390	6.3	0.4	6.9	0.4	6.3	1.7	6.6	2.5	0.6	41
A1689	10.8	0.3	10.7	0.3	10.7	1.4	10.3	1.5	0.5	36

Notes: The exposures are the median exposure time in each super mosaic in kiloseconds (ks). The sensitivities represent  $1\sigma$  errors of the aperture photometry.

the intrinsic 850  $\mu\text{m}$  fluxes of the SMGs to be lower than the confusion limit ( $\sim 2\text{ mJy}$ ) based on their discovered locations and the lensing models. We tuned our observations to the low spectral resolution mode (32 frequency channels per chunk) with local oscillator frequency at 343 GHz, so we label our observations as 870  $\mu\text{m}$ .

We summarize our data in Table 1. In Column 1, we give the source IDs, which are used in the rest of the paper; in Column 2, the SCUBA source name from Cowie et al. (2002) or Knudsen et al. (2008); in Column 3, the dates when the SMA tracks were observed; in Column 4, the beam size; in Column 5, the beam position angle; in Column 6, the r.m.s. value of the dirty map at the phase center ( $\sigma$ ); in Column 7, the flux calibrator(s); in Column 8, the passband calibrator(s); and in Column 9, the gain calibrators.

We used the data reduction package MIR to calibrate the visibilities. The visibility data were first weighted by the system temperatures ( $T_{\text{sys}}$ ). Then the bandpass responses were measured and corrected through observations of bright quasars (Column 8). The phase changes were monitored using neighboring known point sources (Column 9). Given that all observations were conducted under good weather conditions with Precipitable Water Vapor (PWV) of  $\leq 1\text{ mm}$ , the phases are stable, and the phase calibrations using multiple (mostly two) calibrators agree with each other. We used planets for the flux calibration. The typical uncertainty of the flux calibration is  $\sim 10\%$ .

We used the calibrated visibilities to produce the images through the MIRIAD routines (Sault et al. 1995). We combined the visibilities from all the available tracks for each source. We used the routine INVERT with natural weighting on the baselines to perform the inverse Fourier transformations on the visibilities in order to produce the dirty maps and the synthesized dirty beam images with  $0''.2$  grids. The natural weighting scheme provides the best signal-to-noise ratio (S/N) at the cost of no sidelobe suppression and slightly poorer resolution. The typical FWHM of our synthesized beam is  $\sim 2''$ . We also performed multi-frequency synthesis during the inverse Fourier transformations, which gives better coverage in the frequency-dependent uv coordinate.

We plotted the histogram of the pixel values of the dirty maps within the primary beam (FWHM  $\sim 37''$ ) and identified significant excess positive signals. We found that detections at any positions with  $S/N > 3.8\sigma$  can be claimed to be robust, where the noise used to generate the S/N maps is the r.m.s. of the dirty maps (given in Column 6 of Table 1). As an example, in Figure 1, we show the histogram of the S/N map of Chen-3, along with the ideal Gaussian distribution having r.m.s. of 1 (green

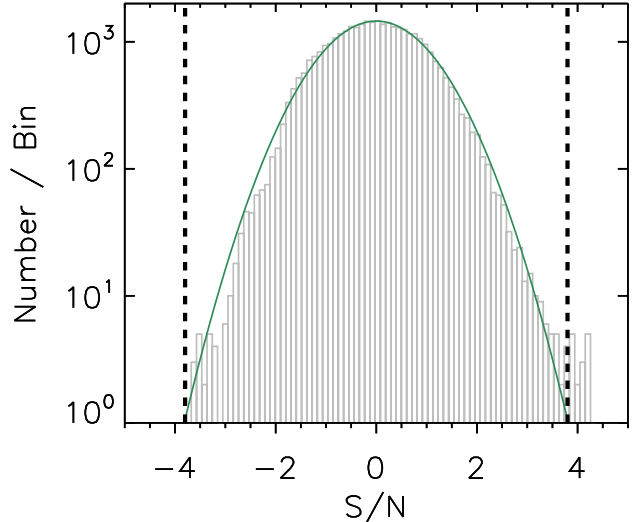


FIG. 1.— S/N histogram of Chen-3 for the pixels located within the SMA primary beam. The S/N map is generated by dividing the dirty maps by the r.m.s. values of the dirty maps. The green curve shows the ideal Gaussian distribution having r.m.s. of 1, and the dashed vertical lines mark  $\pm 3.8\sigma$ . This figure shows that the detection threshold of  $S/N > 3.8\sigma$  used in this paper is robust.

curves). We generated the histogram using the the r.m.s. value of the dirty map ( $\sigma$ ; lower panel), and apparently sources with  $S/N > 3.8\sigma$  are robust detections in our maps.

After identifying the detections, we then performed a deconvolution on the dirty map using the CLEAN routine on the identified source. We CLEANed the area around the detection within an approximately  $5''$  box centered at the peak of the source to around  $1.5\sigma$ . Note that the size of the box was chosen to be large enough to include all real emission but not too big to enclose spurious noise spikes, which would contaminate the real signals in the CLEAN process. Note also that the resulting source fluxes are not sensitive to the depth to which we chose to clean. We then repeated the process on the residual maps with the identified sources removed to look for sources that may appear after CLEANing. We iterated this process until there were no excess signals, meaning the S/N distribution agrees with that of pure noise.

We primary beam-corrected the fluxes of the CLEANed sources by dividing the CLEANed fluxes by the off-axis gain. We used the IMFIT routine to fit the primary beam-corrected signals to a clean beam—an elliptical Gaussian fitted to the central lobe of the dirty beam—to obtain the fluxes and positions of the detected

TABLE 3  
THE PROPERTIES OF THE SMA OBSERVED SOURCES

I.D.	SMA R.A. (J2000) (h m s)	SMA Decl. (J2000) (d m s)	SCUBA R.A. (J2000) (h m s)	SCUBA Decl. (J2000) (d m s)	SCUBA 850 $\mu\text{m}$ (mJy)	SCUBA-2 850 $\mu\text{m}$ (mJy)	SMA 870 $\mu\text{m}$ (mJy)
Chen-1	...	...	02 39 53.83	-01 33 37.0	2.17 $\pm$ 0.57	-0.01 $\pm$ 0.51	<2.52 (4 $\sigma$ )
Chen-2	21 53 35.16	17 41 06.1	21 53 35.48	17 41 09.3	3.24 $\pm$ 0.78	2.35 $\pm$ 0.51	3.96 $\pm$ 1.01
Chen-3	21 53 34.37	17 42 01.5	21 53 34.15	17 42 02.3	2.64 $\pm$ 0.72	1.93 $\pm$ 0.51	4.72 $\pm$ 0.89
Chen-4	...	...	13 11 28.6	-01 20 36	2.6 $\pm$ 0.8	-0.95 $\pm$ 0.48	<3.72 (4 $\sigma$ )
Chen-5	13 11 29.22	-01 20 44.5	13 11 29.1	-01 20 49	4.7 $\pm$ 0.8	4.39 $\pm$ 0.48	5.25 $\pm$ 0.87
Chen-6	13 11 31.93	-01 19 55.1	13 11 32.0	-01 19 55	3.3 $\pm$ 1.0	3.28 $\pm$ 0.50	2.73 $\pm$ 0.81
Chen-7	...	...	13 11 34.1	-01 20 21	3.2 $\pm$ 1.0	4.32 $\pm$ 0.52	<2.56 (4 $\sigma$ )
Chen-8	13 11 34.95	-01 20 17.2	13 11 35.1	-01 20 18	4.9 $\pm$ 1.6	4.15 $\pm$ 0.54	3.92 $\pm$ 0.99

sources. The errors from IMFIT correlate with the noise of the CLEANed maps and with the signal-to-noise ratio of the detections. For each detection, we determined both point-source sensitivities from the dirty maps, and the errors from IMFIT; however, we adopt the errors from IMFIT for our subsequent detailed analysis of each individual source, since they are more realistic. Given the small size of the synthesized beam along with the high S/N of our detections, the typical positional uncertainties of our sources are very small (0".2–0".3 in both R.A. and Decl.), which is critical to estimating the amplifications of strongly lensed sources (Chen et al. 2011).

### 2.2. SCUBA-2 Observations

Recently, we have conducted single-dish 850  $\mu\text{m}$  surveys on all three massive lensing cluster fields using the novel camera SCUBA-2 (Holland et al. 2013) mounted on the JCMT. SCUBA-2, the successor to SCUBA, has an order of magnitude faster mapping speed thanks to a two orders of magnitude increase in the total number of bolometric detectors. Its greatly enhanced imaging capability at both 850  $\mu\text{m}$  and 450  $\mu\text{m}$  makes it possible to take deep submillimeter images with excellent efficiency. Even with only 10–15 hours of observing time, the SCUBA-2 maps of all three fields reach similar depths to the SCUBA maps but with a factor of 20 more sky coverage. The SCUBA-2 observations can therefore provide independent measurements of our sample sources. The details of the SCUBA-2 observations and data reduction can be found in Chen et al. (2013a,b).

### 2.3. Hubble Space Telescope and Spitzer Space Telescope Observations

We also made use of archival data from the *Hubble Space Telescope* (hereafter, *HST*) and the *Spitzer Space Telescope* (hereafter, *Spitzer*). The A370 Advanced Camera for Surveys (ACS) images were taken using the F475W, F625W, and F814W filters with around 6.8 ks, 2.0 ks, and 3.8 ks of exposure (PID: 11507). The ACS F850LP filter was used to take images of A2390 with  $\sim$ 6.4 ks of exposure (PID: 10504), and the ACS F814W filter was used to take images of A1689 with  $\sim$ 10.7 ks of exposure (PID: 11710). We measured the aperture photometry of our SMA detections on the NIR images taken by the Wide Field Camera 3 (WFC3) using the F125W filter. The WFC3 F125W images are, however, only available on A2390 (PI: J. Rigby; PID: 11678) and A1689 (PI: H. Ford; PID: 11802). We estimated the sensitivities of the F125W images using Gaussian fits to

the fluxes measured using 1" radius aperture at random source-free positions, yielding 1  $\sigma$  values of 26.3 and 26.0 AB magnitude for A2390 and A1690, respectively.

We retrieved the Super Mosaics, the enhanced data products generated by the Spitzer Science Center (SSC), of all three fields from the *Spitzer* archive. The Super Mosaics are produced by combining individual *Spitzer* observations and provide the deepest *Spitzer* images possible from the archive. We made use of the Super Mosaics from the Infrared Array Camera (IRAC) at 3.6, 4.5, 5.8, and 8  $\mu\text{m}$ , and the Multiband Imaging Photometer of *Spitzer* (MIPS) at 24  $\mu\text{m}$ . We list the median exposure times for each field in Table 2. Throughout this paper, we measure the source fluxes and the upper limits using circular apertures with diameters of 4".8, 4".8, 6".0, 6".0, and 18".0 at 3.6, 4.5, 5.8, 8.0, and 24  $\mu\text{m}$ , which are roughly three times the FWHM of the PSFs (Fazio et al. 2004; Rieke et al. 2004). We estimated the sensitivities using Gaussian fits to the fluxes measured at random source-free positions. We give the 1  $\sigma$  limits in Table 2, all in  $\mu\text{Jy}$ .

### 2.4. Very Large Array Observations

Deep VLA data were taken at 1.4 GHz using the A configuration (A2390) and both the A and B configuration (A370). The A2390 (A370) image reaches a 1  $\sigma$  noise level of 5.6 (5.7)  $\mu\text{Jy}/\text{beam}$  around the cluster regions with a synthesized beam of  $\sim$ 1".4 (1".7). The details of the radio images can be found in Wold et al. (2012).

We also make use of the archival VLA image at 1.4 GHz of A1689 (PID: AB879). This image is much shallower than the A2390 and A370 images (1  $\sigma$   $\sim$ 0.15 mJy/beam) with a larger synthesized beam of  $\sim$ 6".

### 2.5. LENSTOOL

Throughout this paper, we use LENSTOOL (Kneib et al. 1996) which models three-dimensional mass distributions within the cluster, to de-lense the sources on the image plane to the source plane in order to calculate the magnification factors due to lensing. We adopted the latest LENSTOOL mass models of A370 ( $z = 0.38$ ), A1689 ( $z = 0.18$ ), and A2390 ( $z = 0.23$ ) from Richard et al. (2010a), Limousin et al. (2007), and Richard et al. (2010b). The total number of mass components adopted in the lensing models of A370, A1689, and A2390 are 60, 192 and 50, respectively. Note that there are many other mass models available, especially for A370 and A1689, both in the literature (e.g., Coe et al. 2010) and on the

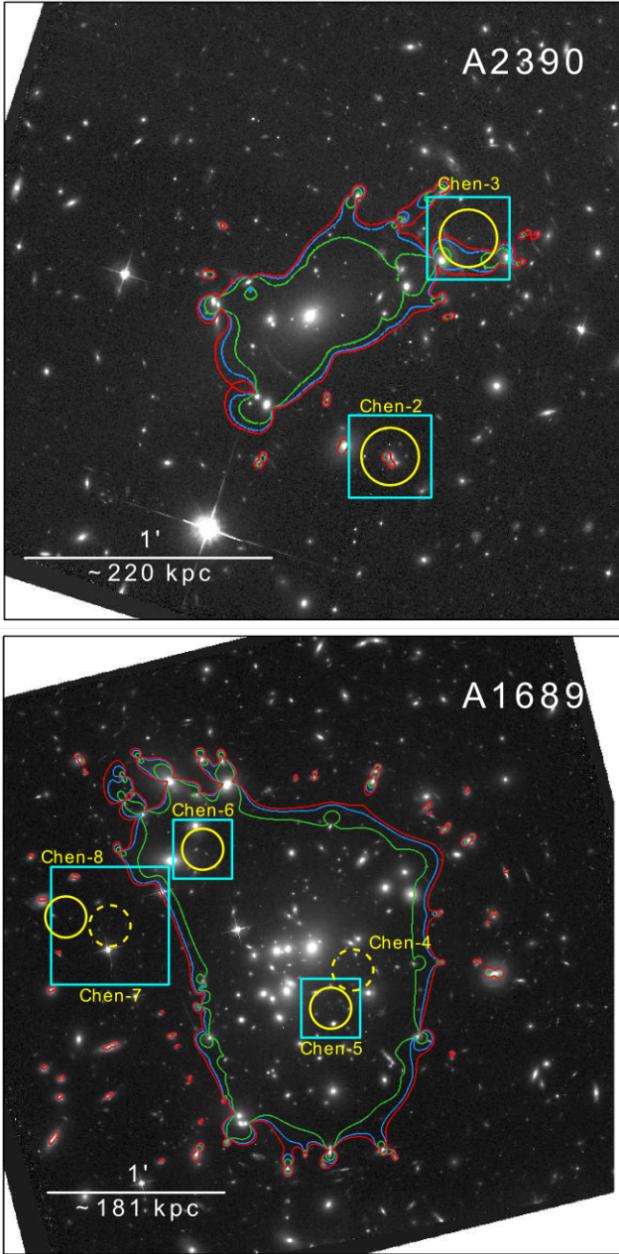


FIG. 2.— Two optical images centered on the brightest cluster galaxy (BCG) of the massive galaxy clusters A2390 and A1689. In each panel, the critical lines at  $z = 2, 4, 6$  are drawn as green, blue and red curves, respectively. The SMA observed SCUBA sources are marked in yellow. The SCUBA sources that are SMA detected (undetected) are denoted by solid (dashed) circles. The cyan squares outline the regions where zoom-in images will be presented later in the paper. The radius of the circles is  $7''0$ , which matches the size of the SCUBA beam FWHM.

publicly available Hubble Frontier Fields website<sup>7</sup>.

We also note that lensing magnifications ( $\mu$ ) can be sensitive to the cluster mass models, in particular in strong lensing regions with  $\mu > 10$ , where the values can be scattered by a factor up to 40% due to the degeneracy of different mass model fits (Coe et al. 2010). However, as we show in the discussion section, our main conclusion is not sensitive to this uncertainty.

<sup>7</sup> <http://archive.stsci.edu/prepds/frontier/lensmodels/>

### 3. RESULTS

We obtained SMA detections of 5 of the 8 observed SCUBA sources. We summarize our results in Table 3. Two of the three SMA undetected SCUBA sources, Chen-1 and Chen-4, are also not detected in the latest SCUBA-2 observations. Both were detected at less than the  $4\sigma$  level in the SCUBA data, and we therefore conclude that they are likely to be spurious. The other SMA undetected source, Chen-7, which is detected in both the SCUBA and SCUBA-2 observations, could be composed of multiple faint sources that are below our current SMA detection limit (more detail in Section 3.3). In Figure 2, we show the optical images of A2390 and A1689 with the targeted SCUBA sources marked in yellow. We denote which of the SCUBA sources were SMA detected or undetected by using solid or dashed circles, respectively. We outline the regions with cyan squares where we will be presenting zoom-in images later. Below we describe each detection in detail.

#### 3.1. *Chen-2*

In Chen et al. (2011), we reported that Chen-2 (named A2390-3 in Chen et al. 2011) had resolved into two distinct sources, Chen-2a and Chen-2b, located close to one another with a projected angular distance of a few arcseconds. After reanalyzing the maps by CLEANing one source at a time, as opposed to CLEANing both sources together, we found that the significance of the Chen-2b detection dropped below  $3\sigma$ . It is likely that Chen-2b is a noise peak boosted by the sidelobes of the real detection, Chen-2a. We therefore revise our results for Chen-2 and present it as a single source detection in Table 3.

We show postage stamp images of Chen-2 in Figure 3, centered at the original SCUBA position from Cowie et al. (2002), with the SMA detection denoted by a yellow circle. As we discussed in Chen et al. (2011), the fact that Chen-2 is not detected in any other waveband, and, in particular, in the radio, indicates that this source could be a high-redshift faint SMG. Radio data are usually an excellent tracer for SMGs, thanks to the well-known empirical correlation between non-thermal radio emission and thermal dust emission among star-forming galaxies (Condon 1992). Moreover, while the submillimeter flux remains almost invariant over the redshift range  $z \sim 1 - 8$  due to a negative  $K$ -correction (Blain et al. 2002), the radio flux drops at high redshifts due to a positive  $K$ -correction. Thus, millimetric redshifts can be estimated from the radio to submillimeter flux ratios with the assumption of a local template spectral energy distribution (SED) (e.g., Carilli & Yun 1999; Barger et al. 2000; Ivison et al. 2002; Barger et al. 2012; Chen et al. 2013a). While dust properties, such as temperature and emissivity, could in principle cause uncertainties in the millimetric redshifts, it is not known how much and in what way. Reassuringly, Barger et al. (2012) found that their millimetric redshifts agreed well with the spectroscopic redshifts for their SMA observed SMGs, in particular at  $z > 3$ , where the uncertainties are mainly due to the errors in the flux measurements.

We estimate the millimetric redshift of Chen-2 by assuming the SED of the local starbursting galaxy Arp 220 ( $T_d = 47\text{ K}$ ,  $\beta=1$ ). Because Chen-2 is not detected in the deep VLA map, we use the  $3\sigma$  radio flux upper limit of

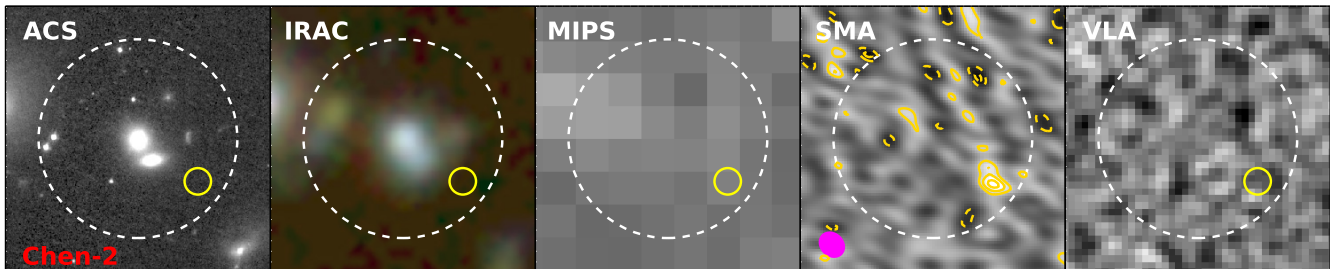


FIG. 3.— Postage stamp images centered on the SMA phase center position of Chen-2, which is the original SCUBA centroid from Cowie et al. (2002). From left to right:  $20'' \times 20''$  gray scale ACS f850lp, IRAC false color (r-g-b)  $8.0\text{-}5.8\text{-}3.6\ \mu\text{m}$ , and gray scale MIPS  $24\ \mu\text{m}$ , SMA  $870\ \mu\text{m}$ , and VLA  $1.4\ \text{GHz}$  images. In each panel (except SMA), we denote the SMA detection by a  $1''$  radius yellow circle. In the SMA panel, the contours are  $(-3, -2, 2, 3, 4) \times \sigma$ , and the synthesized beam is presented in the bottom-left corner (magenta). North is up and East is to the left. The white dashed circle in each panel shows the  $7.5''$  radius SCUBA beam.

$16.8\ \mu\text{Jy}$ . Based on Equations 2 and 4 in Barger et al. (2000), the millimetric redshift of Chen-2 is then  $> 3$ . Thanks to the two cluster members close to the center of the SCUBA beam, Chen-2 is strongly amplified by a factor of  $4.8^{+0.5}_{-0.25}$ , where the errors represent the uncertainties on the positions ( $\pm 0''.2$ ) and redshifts ( $3 < z < 6$ ). The intrinsic (de-lensed)  $870\ \mu\text{m}$  flux is  $0.8 \pm 0.25\ \text{mJy}$ . Assuming an Arp 220 SED, the total IR luminosity ( $8\text{-}1000\ \mu\text{m}$ ) of Chen-2 would be  $6.2 \times 10^{11} - 1.1 \times 10^{12}\ L_{\odot}$ .

### 3.2. Chen-3

Chen-3 was first detected by Cowie et al. (2002) (source #14 in Cowie et al. 2002) with an  $850\ \mu\text{m}$  flux of  $2.64\ \text{mJy}$ . Using ISOCAM, Metcalfe et al. (2003) also reported detections at  $7$  and  $15\ \mu\text{m}$  of the arc structure enclosed by the SCUBA beam. The forbidden cooling line [O II] ( $3727\ \text{\AA}$ ) was identified toward this arc by Pello et al. (1991), indicating a star-forming galaxy at  $z = 0.913$  and a very likely counterpart for Chen-3. However, our SMA observations reveal a different story.

In Figure 4, we show postage stamp images of Chen-3 with the SMA detection denoted by a yellow circle. The only candidate counterpart to Chen-3 is the IRAC and MIPS detections north-east of the SMA position and located within the SCUBA beam (white dashed circle). However, referring to the ACS image, it is more likely that the IR candidate counterpart traces part of the optical arc instead of the submillimeter signal from Chen-3, based on the fact that the morphology of the IR signal is elongated (aligned with the arc), and the positional offset is much greater than the positional error measured from the SMA.

Again, surprisingly, we do not see any counterpart to this faint SMG at other wavelengths. A non-detection in the deep radio map ( $3\sigma$  of  $16.8\ \mu\text{Jy}$ ) gives a millimetric redshift of  $z > 3.5$ . Due to its close proximity to the critical lines (Figure 2), Chen-3 is highly amplified by a factor of at least 45, considering its positional ( $\pm 0''.2$ ) and redshift ( $3.5 < z < 6$ ) uncertainties. We therefore adopt 45 as the nominal amplification of Chen-3. We caution that, as stated in Section 2.5, because Chen-3 is located at a position very close to the critical lines, the scatter of the magnifications could be large. However, given its position close to the cluster center and its alignment with the orientation of the cluster mass distribution, the minimum amplification is likely to be larger than 2, which makes Chen-3 likely to be a faint SMG

with an intrinsic flux  $< 2\ \text{mJy}$ .

Interestingly, although Chen-3 is expected to be highly amplified and stretched, the source itself appears to be point-source-like. In Figure 5, we show the flux versus the  $uv$  distance for Chen-3. A flat trend indicates that the source is unresolved. It could be that Chen-3 is extremely compact and that the current resolution is not sufficient to resolve the source.

By adopting an amplification factor  $> 45$ , Chen-3 has an intrinsic  $870\ \mu\text{m}$  flux of  $< 0.12\ \text{mJy}$ . Again assuming an Arp 220 SED and a redshift of  $3.5 < z < 6$ , Chen-3 has a Milky Way like total IR luminosity of  $< 10^{11}\ L_{\odot}$ . If its low intrinsic IR luminosity were to be confirmed, Chen-3 would be a source with a relatively modest luminosity that is completely hidden from deep optical/NIR/radio observations. Sources like Chen-3 would be completely missed in current optical/NIR calculations of the cosmic star formation history; however, given the amount of light in the faint SMG population, they would contribute comparable amounts of star formation.

### 3.3. Chen-4, 5, 6, 7, 8

The SCUBA discoveries of Chen-4, 5, 6, 7, and 8 were first reported by Knudsen et al. (2008), where they were called SMM J131128.6-012036, SMM J131129.1-012049, SMM J131132.0-011955, SMM J131134.1-012021, and SMM J131135.1-012018, respectively. Chen-4/Chen-5 and Chen-7/Chen-8 are two source pairs that are located close to one another. The fluxes of Chen-5, Chen-6, and Chen-7 were suspected by Knudsen et al. to be contributed by a combination of lensed multiple images of two background sources at  $z \sim 2.6$ , denoted as source #5 and source #24 in the study of the A1689 mass model (Limousin et al. 2007). We show the positions of the multiple images in Figure 6 as cyan circles with the identifications (background source number dot multiple image number) marked. Only one SMA detection (Chen-5) is aligned with a lensed multiple image (5.2).

Based on the mass model of Limousin et al. (2007), the magnification of image 5.1 is  $\sim 2.5$  times higher than that of image 5.2. If the background source is indeed the origin of the submillimeter emission, then we should detect a submillimeter flux toward 5.1 that is stronger than what we observe. Our lack of an SMA detection of image 5.1 could imply that the submillimeter emission is not related to the background source #5. However, we do observe faint submillimeter emission at the positions of images 5.1 and 5.3, so the lack of significant detections

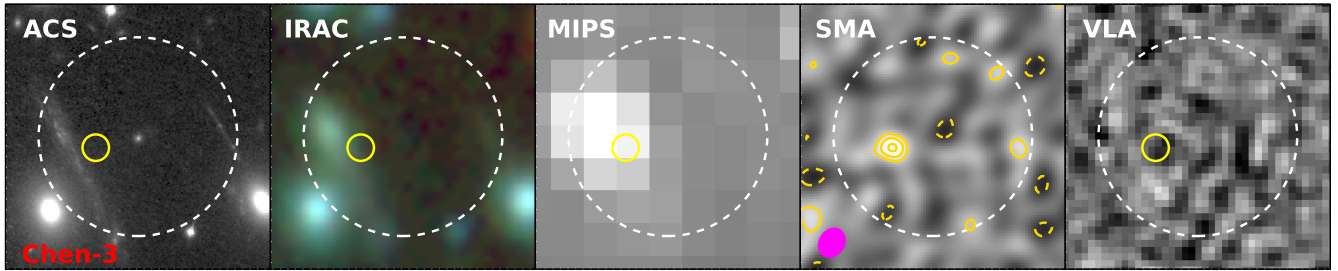


FIG. 4.— Same as Figure 3, but for Chen-3.

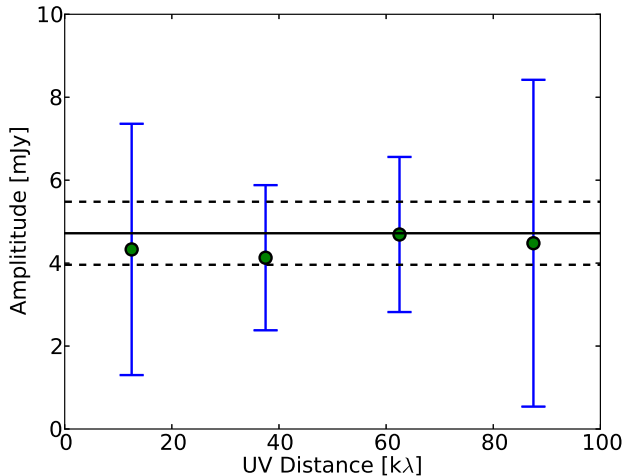


FIG. 5.— Real amplitude in mJy vs. the  $uv$  distance for Chen-3. The black solid line represents the primary beam corrected fluxes obtained using IMFIT on the CLEANed image, and the dashed lines show the  $1\sigma$  errors.

could also be caused by noise.

Alternatively, the lensing magnifications of images 5.1 and 5.2 are subject to large uncertainties due to degeneracies of the mass models, so the lack of a detection on image 5.1 could also be caused by the lensing uncertainties. With more data on the background galaxies and multiple images in A1689, Coe et al. (2010) also computed magnification estimates on images 5.1 and 5.2. Although their final adopted values are similar to those obtained using the model of Limousin et al. (2007) in the sense that image 5.1 is amplified by a larger factor than that of image 5.2, Coe et al. (2010) found that among their ensemble of models, the mean magnification of image 5.2 (5b in Coe et al. 2010) was larger than that of image 5.1 (5a in Coe et al. 2010), with a scatter of  $\sim 50\%$  on both values.

We examine the possibility that source #5 is the counterpart of the submillimeter emission by measuring the submillimeter fluxes at the nominal positions of the multiple optical images of source #5 and comparing their de-lensed fluxes. If the submillimeter emission comes from the same background source, then the de-lensed fluxes should be the same within the errors. We include both the uncertainties on the flux measurements and the uncertainties on the magnification estimates ( $\sim 50\%$ ; Coe et al. 2010) in our error calculations. We show the results in Figure 7: the de-lensed  $870\ \mu\text{m}$  fluxes of the mul-

tipole optical images are indeed the same within errors. We thus conclude that the lensed images 5.1 and 5.2 of background source #5 are likely to be the counterparts of submillimeter source Chen-5 and that the lensed image 5.3 contributes to Chen-7. With the constraints from the multiple measurements, we find the best fit intrinsic  $870\ \mu\text{m}$  flux of Chen-5 is  $0.085 \pm 0.035\ \text{mJy}$  (black line in Figure 7 with errors in dashed lines). At  $z = 2.6$ , the total IR luminosity of Chen-5 is  $\sim 8.5^{+3.5}_{-3.5} \times 10^{10} L_{\odot}$  assuming an Arp 220 SED.

The neighboring pair system Chen-7 and Chen-8 is detected in both the SCUBA and SCUBA-2 observations with consistent flux measurements (Table 3). Interestingly, we only detect Chen-8 with the SMA. The fact that Chen-7 is detected in both the SCUBA and SCUBA-2 observations but not in the SMA observations suggests that it may be composed of multiple faint sources that are below our current SMA detection limit. This would include image 5.3 which, based on the lensing discussion above, would have an observed  $850\ \mu\text{m}$  flux of  $\sim 1\ \text{mJy}$ .

Chen-8 is detected by all three independent observations (SCUBA, SCUBA-2, and SMA). We find counterparts in the IRAC and MIPS images. We also find low surface brightness extended emission in the NIR images obtained from *HST* WFC3 toward the SMA position. We show the zoomed-in inverse grey scale F140W image in Figure 8. We mark the SMA synthesized beam shape with a yellow circle. While the IR emission seen in the IRAC and MIPS images could be contributed by both the point source to the south-east and the extended structure, it is perhaps more likely that most of the submillimeter flux comes from the extended structure, given the SMA position and its optically faint nature. Due to the fact that the IR fluxes are contributed by both the bright point source and the extended structure, it is unrealistic to estimate the photometric redshift of Chen-8 using the IR flux measurements. However, based on the fact that it is not detected in the radio images with  $3\sigma = 0.45\ \text{mJy}$ , we can put a lower limit on its redshift as  $z > 0.5$ . Chen-8 is also strongly amplified by a factor of 3–9, depending on its redshift from  $z = 0.5$ –6. The intrinsic fluxes of the IR counterparts are 22.1–23.3, 21.6–22.8, 21.4–22.6, 21.4–22.6, and 19.4–20.6 in AB magnitudes or 1.8–5.4, 2.7–8.0, 3.2–9.6, 3.3–9.9 and 20–60  $\mu\text{Jy}$  at 3.6, 4.5, 5.8, 8.0 and 24  $\mu\text{m}$  for the same redshift range. By adopting the nominal amplification of 6, the intrinsic  $870\ \mu\text{m}$  flux would be  $0.65^{+0.86}_{-0.28}\ \text{mJy}$ , and assuming an Arp 220 SED the total IR luminosity would be  $\sim 4\text{--}6 \times 10^{11} L_{\odot}$ .

Chen-6 was first discovered by Knudsen et al. (2008) and the detection is confirmed by both our SCUBA-

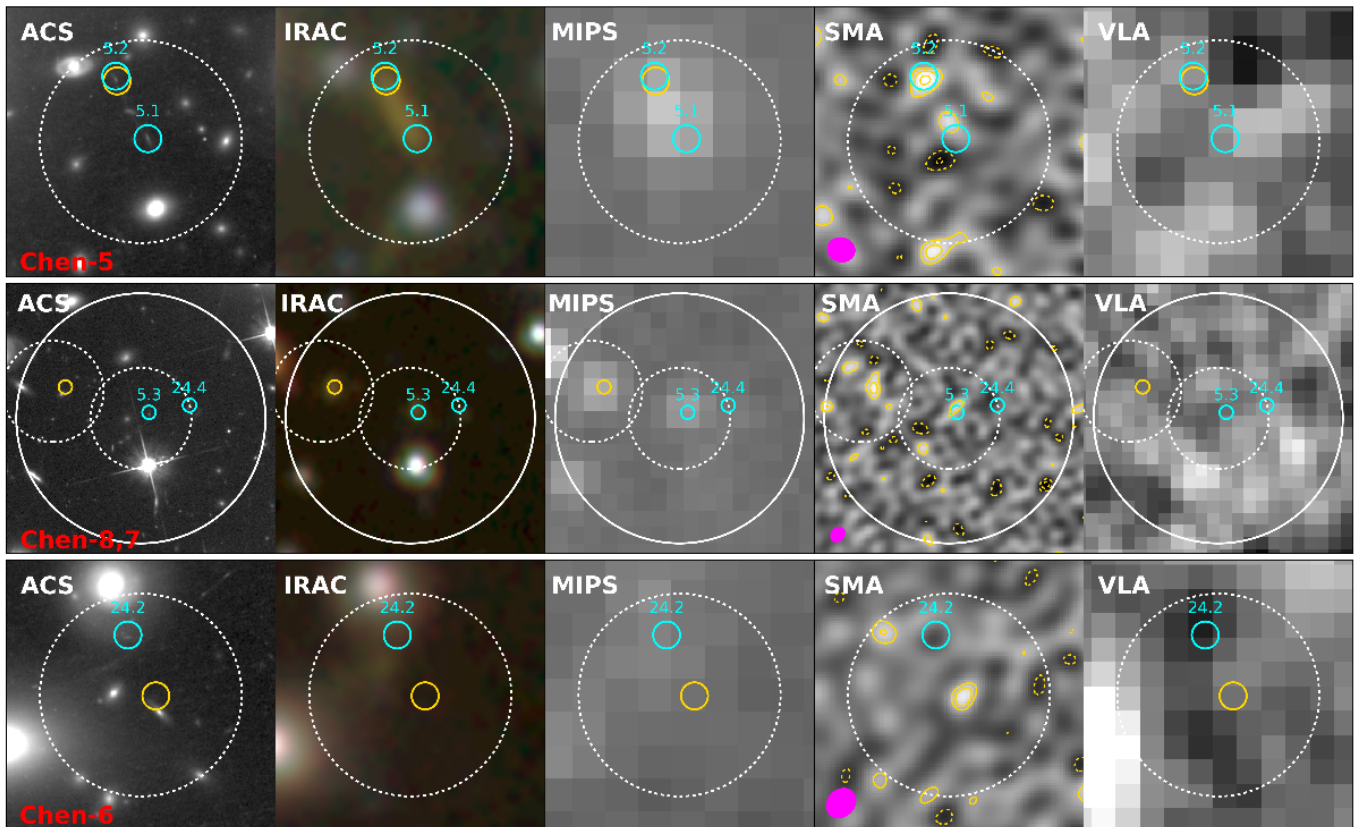


FIG. 6.— Postage stamp images of (top row) Chen-5, (middle row) Chen-7 and Chen-8, and (bottom row) Chen-6. The white dashed circles show  $7''.5$  radius SCUBA beams. The middle row contains two SCUBA sources: Chen-7 (center) and Chen-8 (left). Here, the size of each panel is adjusted to  $40'' \times 40''$  to enclose both sources. For the other two rows, the size of each panel is  $20'' \times 20''$ . The white large solid circle shows the size of the SMA primary beam with 50% sensitivity relative to the phase center. The yellow circles mark the SMA detections. The cyan circles mark the positions of the multiple images from background sources 5 and 24, as labeled. The optical image is from the ACS filter F814W.

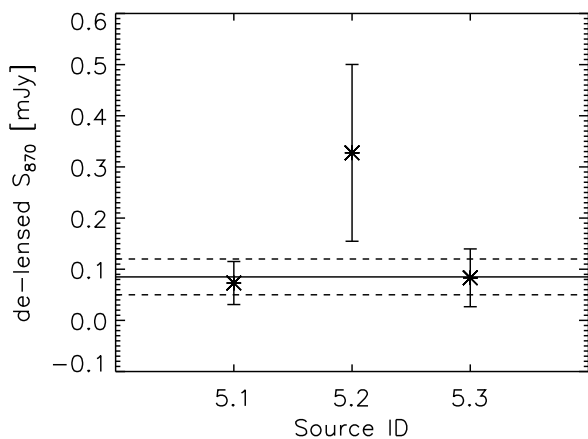


FIG. 7.— De-lensed  $870\ \mu\text{m}$  fluxes with  $1\ \sigma$  errors obtained by de-lensing the measured submillimeter fluxes at the nominal positions of the multiple optical images of the background source #5. The best fit de-lensed flux is shown with the black line, while the errors are plotted with dashed lines. The magnifications adopted in this calculation are 31.9, 12.8 and 11.6 for images 5.1, 5.2, and 5.3, respectively.

2 and SMA observations with consistent flux measurements. We mark the SMA sources in yellow in the bottom row of Figure 6. Interestingly, it is not located close

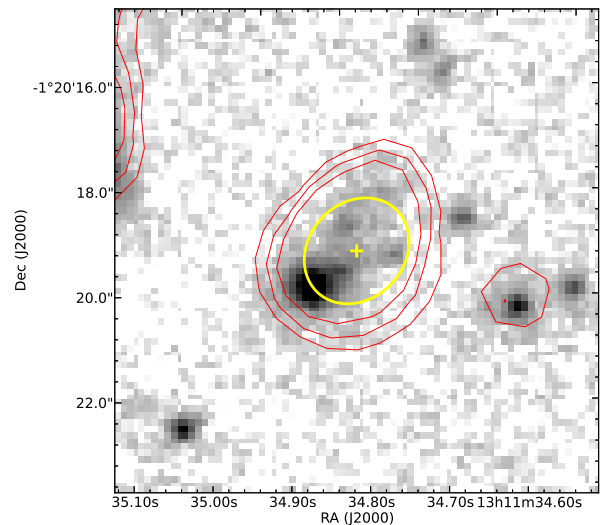


FIG. 8.— Zoomed-in inverse grey scale F140W image of Chen-8 with red contours representing the  $3.6\ \mu\text{m}$  IRAC emission. The shape of the SMA synthesized beam is shown with the yellow circle. The yellow cross marks the SMA position with the positional errors shown in its length. The angular width of this map is  $10''$ .

to the lensed multiple image of the background source #24, which was suspected by Knudsen et al. (2008) to be the main contributor of the observed submillimeter flux.



Moreover, as we see in most of our SMA detections, there is no obvious counterpart found in observations at any other wavelength. There is an optical candidate counterpart lying on the edge of the beam; however, it is unlikely to be the true counterpart, since it is optically bright but IR faint, and the positional offset is significant.

Chen-6 lies close to two massive cluster members, seen in the figure lying just outside the white dashed circle, and is strongly magnified. Again, the lack of a radio detection for Chen-6 implies that it is a background source behind the cluster ( $z > 0.5$ ). Although without the redshift information it is hard to determine the amplification factors for sources that are strongly magnified, we can determine lower limits, as we did for Chen-3. The lower limit is 10 over the redshift range  $z = 0.5\text{--}6$  for Chen-6, which gives the intrinsic  $870\ \mu\text{m}$  fluxes of  $<0.34\ \text{mJy}$ . Assuming an Arp 220 SED, the total IR luminosity of Chen-6 would be  $<4 \times 10^{11}\ L_{\odot}$ .

#### 4. DISCUSSION

Because the positions of the single-dish detected SMGs are poorly determined, accurately finding the true SMG counterparts is critical for understanding their characteristics. Since SMGs are dusty and their emission appears to be dominated by star formation (e.g., Alexander et al. 2005), sources detected in *Spitzer* MIR and VLA images with better determined locations are often used to cross-identify the SMG counterparts (e.g., Ivison et al. 2007; Biggs et al. 2011). However, both MIR and radio fluxes drop significantly at high redshifts, while the  $850\ \mu\text{m}$  fluxes remain almost invariant over the redshift range  $z = 1\text{--}8$  due to the negative  $K$ -correction (Blain et al. 2002). Many high-redshift, dusty sources are inevitably missed in flux-limited observations at MIR and radio wavelengths.

Recently, observations using ALMA with arcsecond level spatial resolution have successfully pinpointed the location of a flux-limited sample of  $\sim 100$   $870\ \mu\text{m}$  SMGs selected by the LABOCA survey in the ECDF-S field (Hodge et al. 2013). Armed with accurate positions, Hodge et al. tested the robustness of the counterpart identifications made with MIR and radio data by Biggs et al. (2011). They found that only 45 out of their 99 robustly detected sources (ALESS MAIN) had robust MIR/radio counterparts; the recovery rate increased to  $\sim 55\%$  if they included tentative MIR/radio identifications.

Interestingly, if we separate the Hodge et al. sample into flux bins, then the fraction of SMGs with robust MIR/radio counterparts (black circles in Figure 9) dramatically decreases for bins fainter than  $3\ \text{mJy}$ . Our sample extends even fainter, and we obtain a similarly low fraction (2 out of our 6 SMA sources have MIR/radio counterparts; blue circle in Figure 9). Note that the depth of the MIR/radio images is key to the results shown in Figure 9, as we expect that more sources could be recovered with deeper images. Indeed, Barger et al. (2012) recently showed that all their bright SMGs with  $860\ \mu\text{m}$  fluxes above  $3\ \text{mJy}$  are recovered by ultra-deep  $1.4\ \text{GHz}$  images ( $1\sigma \sim 2.5\ \mu\text{Jy}$ ).

With the strong gravitational lensing (amplification  $> 5$ ), the *Spitzer* images in our source fields ( $1\sigma$ ;  $<0.08$ ,  $<0.08$ ,  $<0.3$ ,  $<0.5$ , and  $<8\ \mu\text{Jy}$  at  $3.6$ ,  $4.5$ ,  $5.8$ ,  $8.0$ , and  $24\ \mu\text{m}$ ) are deeper than ECDF-S and almost as deep as in GOODS-S, which is one of the deepest *Spitzer* observed

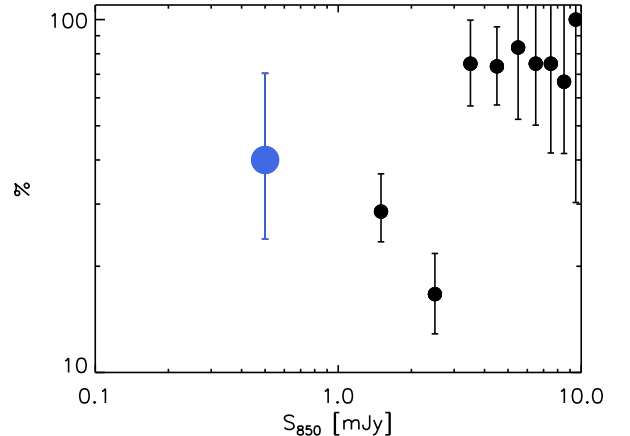


FIG. 9.— The percentage of SMGs in each flux bin robustly identified in MIR/radio images with similar depths to the ECDF-S field. The SMGs shown in this figure were all observed with arc-second resolution submillimeter interferometers. Black circles are from Hodge et al. (2013), and the blue circles shows our work.

fields (Magnelli et al. 2009; Damen et al. 2011).

Similarly, with the strong lensing, our A2390 radio images reach  $1\sigma < 1\ \mu\text{Jy}$  at our source positions, by far the deepest  $1.4\ \text{GHz}$  depth. Even in A1689, where the radio data are shallower, with the lensing, the sensitivity reaches  $1\sigma \sim 10\ \mu\text{Jy}$ , similar to the depth of the ECDF-S (Miller et al. 2008).

We can also see this effect in the optical/NIR regime. We measured  $1''$  radius aperture F125W magnitudes at the SMA positions using the *HST* WFC3 archival images described in Section 2. In Table 4, we summarize these measurements along with other detailed characteristics of each SMA detection, including the magnifications, de-lensed fluxes, and redshifts. We show the histogram of our F125W magnitudes in dark blue in Figure 10, excluding only Chen-8, where there is no F125W imaging. For the cases where there was no detection in F125W, which applies to most of our SMA sources, we calculated the upper limits by taking into account the lensing uncertainties. We corrected all of our measurements to total magnitudes based on the released encircled energy fractions (Table 7.6 in Dressel 2012). We de-lensed them based on the adopted magnifications. We estimated any contamination due to foreground emission from cluster members using pixels with distances between  $1''/2$  and  $1''/4$  from the SMA positions.

For comparison, we show the histogram of the F125W magnitudes of the SMA-detected, bright SCUBA-2 SMG sample with  $860\ \mu\text{m}$  fluxes  $> 3\ \text{mJy}$  given in Barger et al. (2013) (*hatched*), except CDFN1, CDFN2, CDFN3, and CDFN18, where there is no F125W imaging, and GOODS 850-17, where the flux of the source is too contaminated by the neighboring source (Barger et al. 2012). We measured the magnitudes using a  $1''$  radius aperture on the *HST* WFC3 archival images obtained for the Cosmic Assembly Near-IR Deep Extragalactic Legacy Survey (CANDELS; Grogin et al. 2011) by P. S. Faber (PID: 12443, 12444, 12445), except GOODS 850-1, where we used a  $0.5''$  radius aperture to minimize contamination from the neighboring sources. We corrected all of our

TABLE 4  
THE PROPERTIES OF THE SMA DETECTED SOURCES

ID	Magnifications	$S_{870,\text{intrinsic}}$ (mJy)	$S_{F125W,\text{intrinsic}}$ (mag)	$z^b$	$\log(L_{8-1000\mu\text{m}})$
Chen-2	4.8 (4.7–5.3)	0.83 (0.64–0.97)	> 26.8	> 3.0	11.8–12.0
Chen-3	45 (> 45)	0.12 (< 0.12)	> 28.2	> 3.5	< 11.1
Chen-5	19 (16–22)	0.09 (0.05–0.12) <sup>a</sup>	26.6 (26.5–26.8)	2.600	10.7–11.1 <sup>a</sup>
Chen-6	10 (> 10)	0.34 (< 0.34)	> 25.6	> 0.5	< 11.6
Chen-8	6 (3–9)	0.65 (0.37–1.51)	...	> 0.5	11.6–11.8

<sup>a</sup> Mean values based on the measurements on all three multiple images of source #5.

<sup>b</sup> Lower limits are millimetric redshifts estimated using the ratio between the radio and the submillimeter fluxes.

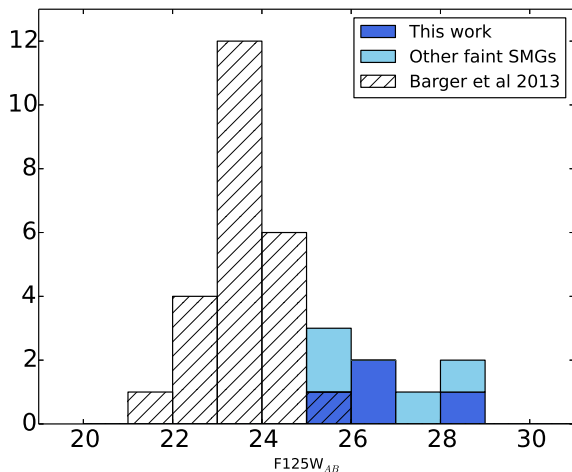


FIG. 10.— Histograms of the intrinsic F125W magnitudes of our faint SMG sample (*dark blue*), other faint SMGs from the literature (Frayer et al. 2003; Kneib et al. 2004; Gonzalez et al. 2009; Knudsen et al. 2010) (*light blue*), and the bright SMG sample from Barger et al. (2013) (*hatched*). The histogram of the faint SMGs is stacked, whereas that of the bright SMG sample is independent from the faint SMGs.

measurements to total magnitudes.

We also show the magnitudes for other faint SMGs in the literature with intrinsic  $870\mu\text{m}$  fluxes  $< 2\text{mJy}$  (*light blue*). These were measured in the  $J$ -band, except for SMM J163555.5+661300, where the closest passband available was the F110W filter of WFC3 (Knudsen et al. 2010).

From Figure 10, we see that, in contrast to the bright SMGs, faint SMGs with  $870\mu\text{m}$  fluxes  $< 2\text{mJy}$  are statistically dimmer with F125W AB magnitudes spanning the range 24–29. We stress that the fact that faint SMGs are statistically dimmer than bright SMGs in the NIR is not affected by the uncertainties of strong lensing. Since the uncertainties of lensing amplifications are affected by many factors, such as the degeneracies of the cluster mass models and the errors in the measurements of the source positions in coordinates and in redshifts, it is difficult to quantify the lensing uncertainties for each individual faint SMG in Table 4. However, if we assume all of our sources have only a lensing magnification of 2, which is very conservative given their proximity to the cluster center, the median de-lensed F125W magnitude of the faint SMGs (25.4 including other faint SMGs from

the literature) is still larger than all the bright SMGs. Moreover, four out of our five F125W measurements are upper limits, the median de-lensed F125W magnitude of faint SMGs is likely to be lower than 25.4.

Our results suggest that a large fraction of the faint SMGs will be missed in NIR surveys having magnitude limits 22–25 (e.g., Quadri et al. 2007; Keenan et al. 2010). This is in agreement with the stacking analysis of Wang et al. (2006), who stacked the GOODS-N SCUBA data at the positions of sources detected in the NIR with an AB magnitude limit of  $\sim 24$ . They found that after excluding the bright SMGs from the maps, they could account for only about one-quarter of the  $850\mu\text{m}$  EBL (based on the EBL measurement of Fixsen et al. 1998) with their combined  $H$ -band and  $3.6\mu\text{m}$  sample and that this light was coming from sources at  $z < 1.5$ . Based on our latest number counts, bright SMGs contribute about another quarter of the  $850\mu\text{m}$  EBL (Chen et al. 2013a,b), which implies that up to 50% of the  $850\mu\text{m}$  EBL is still hidden from deep NIR samples. Similar results were presented by Serjeant et al. (2008), who stacked SCUBA data at the positions of sources detected in *Spitzer* images at  $3.6\mu\text{m}$  ( $1.5\mu\text{Jy}$ ,  $1\sigma$ ),  $4.5\mu\text{m}$  ( $1.5\mu\text{Jy}$ ,  $1\sigma$ ),  $5.8\mu\text{m}$  ( $3\mu\text{Jy}$ ,  $1\sigma$ ),  $8\mu\text{m}$  ( $4\mu\text{Jy}$ ,  $1\sigma$ ) and  $24\mu\text{m}$  ( $9\mu\text{Jy}$ ,  $1\sigma$ ). They also found that after excluding the bright SMGs, they could account for only about one-quarter of the  $850\mu\text{m}$  EBL with their *Spitzer* sample, and, similar to Wang et al. (2006), that this light was dominated by sources at  $z < 1.5$ .

Consistent with these stacking results, studies of  $z < 2$  (U)LIRGs have shown that there is less dust obscuration ( $L_{\text{IR}}/L_{\text{UV}}$ ) in low-luminosity sources (e.g., Chary & Elbaz 2001; Le Floc’h et al. 2005; Reddy et al. 2010), which would suggest that the observed NIR/submm flux ratios should increase as we go from bright SMGs to faint SMGs. This, together with the fact that the lensed faint SMGs are amplified relative to the bright SMGs, leads to the expectation that the observed F125W fluxes of the faint SMGs should be brighter than those of the bright SMGs. However, this is not what we observe.

In Figure 11 (left), we plot the F125W-to- $870\mu\text{m}$  flux ratios versus the observed  $870\mu\text{m}$  fluxes for our SMA detected faint SMGs (diamonds), together with those of the bright SMGs (squares) from Barger et al. (2014). In Figure 11 (right), we de-lense the faint SMGs, plotting their intrinsic fluxes on the x-axis. We also show the empirical predictions (black curves) based on the SED templates of Chary & Elbaz (2001) for redshifts from 1.5 to 6.0. Figure 11 suggests that these faint SMGs must either be at much higher redshifts than what was expected from

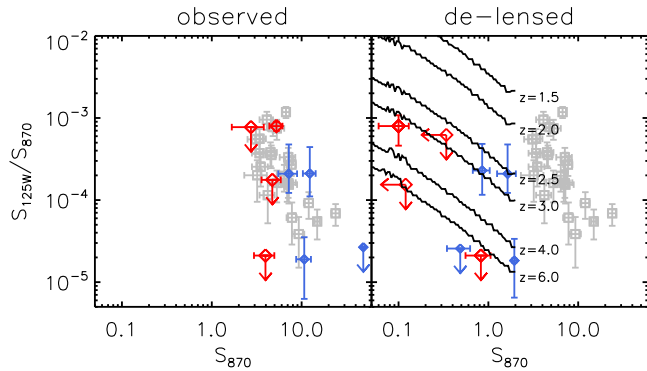


FIG. 11.— The F125W-to-870  $\mu\text{m}$  flux ratios vs. 870  $\mu\text{m}$  fluxes of our SMA detected faint SMGs (*red diamonds*), other faint SMGs from the literature that are the same as those used in Figure 10 (*blue diamonds*), and the bright SMGs (*squares*) adopted from Barger et al. (2014). Three out of our four SMA-detected faint SMGs (no F125W data available for Chen-8; Table 4) are not detected in the F125W maps; thus, we show their upper limits. In the left panel, we plot the flux ratios against the observed 870  $\mu\text{m}$  fluxes, whereas in the right panel, we plot the flux ratios against the de-lensed 870  $\mu\text{m}$  fluxes by adopting the information in Table 4. In the right panel, we also show the empirical predictions (*black curves*) based on the SED templates of Chary & Elbaz (2001) at  $z = 1.5, 2.0, 2.5, 3.0, 4.0,$  and  $6.0$ .

the stacking analyses, or be extremely dusty.

All this evidence suggests that many faint SMGs are optically and NIR faint, and that there is a considerable amount of submillimeter light coming from objects which are fainter than the population probed by most of the current NIR, MIR, and even radio surveys. Our results also suggest that there are many low-luminosity, obscured star forming galaxies at high redshift that do not merge into the normal galaxy population and hence would not be included in the optical star formation history.

## 5. SUMMARY

We conducted SMA observations of 8 faint SMGs detected by SCUBA with intrinsic 850  $\mu\text{m}$  fluxes  $< 2$  mJy. We obtained SMA detections of 5 of the SCUBA sources. Based on the latest number counts, these sources contribute  $\sim 70\%$  of the 850  $\mu\text{m}$  EBL, and they represent the dominant star-forming galaxy population in the dusty universe. We found that the fraction of faint SMGs with MIR/radio counterparts is low,  $40_{-16}^{+30}\%$ , compared with bright SMGs, where the majority have counterparts. We also found that the NIR counterparts of faint SMGs are statistically dimmer than those of bright SMGs, suggesting that many faint SMGs must either be at very high redshifts, or be extremely dusty. Our results also suggest that there are many low-luminosity, obscured star forming galaxies at high redshifts that would not be included in measurements of the optical star formation history.

*Acknowledgments* We thank the referee for comments that improved the manuscript. We gratefully acknowledge support from NSF grants AST-0709356 (C.C.C., L.L.C.), AST-1313309 (L. L. C.), and AST-1313150 (A. J. B.), the University of Wisconsin Research Committee with funds granted by the Wisconsin Alumni Research Foundation (A.J.B.), the David and Lucile Packard Foundation (A.J.B.), and the National Science Council of Taiwan grant 102-2119-M-001-007-MY3 (W.-H.W.). We thank SMA support astronomer Glen Petitpas. This research made use of Astropy, a community-developed core Python package for Astronomy (Astropy Collaboration et al. 2013). The authors wish to recognize and acknowledge the very significant cultural role and reverence that the summit of Mauna Kea has always had within the indigenous Hawaiian community. We are most fortunate to have the opportunity to conduct observations from this mountain.

## REFERENCES

- Alexander, D. M., Bauer, F. E., Chapman, S. C., et al. 2005, *ApJ*, 632, 736  
 Astropy Collaboration, Robitaille, T. P., Tollerud, E. J., et al. 2013, *A&A*, 558, A33  
 Barger, A. J., Cowie, L. L., & Richards, E. A. 2000, *AJ*, 119, 2092  
 Barger, A. J., Cowie, L. L., & Sanders, D. B. 1999, *ApJ*, 518, L5  
 Barger, A. J., Cowie, L. L., Sanders, D. B., et al. 1998, *Nature*, 394, 248  
 Barger, A. J., Wang, W.-H., Cowie, L. L., et al. 2012, *ApJ*, 761, 89  
 Barger, A. J., Cowie, L. L., Chen, C.-C., et al. 2014, *ApJ*, 784, 9  
 Biggs, A. D., Ivison, R. J., Ibar, E., et al. 2011, *MNRAS*, 413, 2314  
 Blain, A. W., Kneib, J., Ivison, R. J., & Smail, I. 1999, *ApJ*, 512, L87  
 Blain, A. W., Smail, I., Ivison, R. J., Kneib, J., & Frayer, D. T. 2002, *Phys. Rep.*, 369, 111  
 Boone, F., Clément, B., Richard, J., et al. 2013, *A&A*, 559, L1  
 Borys, C., Chapman, S., Halpern, M., & Scott, D. 2003, *MNRAS*, 344, 385  
 Borys, C., Smail, I., Chapman, S. C., et al. 2005, *ApJ*, 635, 853  
 Bothwell, M. S., Smail, I., Chapman, S. C., et al. 2013, *MNRAS*, 429, 3047  
 Carilli, C. L., & Yun, M. S. 1999, *ApJ*, 513, L13  
 Casey, C. M., Chen, C.-C., Cowie, L. L., et al. 2013, *MNRAS*, 436, 1919  
 Chapman, S. C., Blain, A. W., Smail, I., & Ivison, R. J. 2005, *ApJ*, 622, 772  
 Chary, R., & Elbaz, D. 2001, *ApJ*, 556, 562  
 Chen, C.-C., Cowie, L. L., Barger, A. J., et al. 2013a, *ApJ*, 762, 81  
 —. 2013b, *ApJ*, 776, 131  
 Chen, C.-C., Cowie, L. L., Wang, W.-H., Barger, A. J., & Williams, J. P. 2011, *ApJ*, 733, 64  
 Coe, D., Benítez, N., Broadhurst, T., & Moustakas, L. A. 2010, *ApJ*, 723, 1678  
 Condon, J. J. 1992, *ARA&A*, 30, 575  
 Coppin, K., Chapin, E. L., Mortier, A. M. J., et al. 2006, *MNRAS*, 372, 1621  
 Cowie, L. L., Barger, A. J., & Kneib, J. 2002, *AJ*, 123, 2197  
 Damen, M., Labbé, I., van Dokkum, P. G., et al. 2011, *ApJ*, 727, 1  
 Dressel, L. 2012, *Wide Field Camera 3 Instrument Handbook for Cycle 21 v. 5.0 (HST Instrument Handbook)*  
 Dye, S., Eales, S. A., Aretxaga, I., et al. 2008, *MNRAS*, 386, 1107  
 Eales, S., Lilly, S., Gear, W., et al. 1999, *ApJ*, 515, 518  
 Eales, S., Lilly, S., Webb, T., et al. 2000, *AJ*, 120, 2244  
 Fazio, G. G., Hora, J. L., Allen, L. E., et al. 2004, *ApJS*, 154, 10  
 Fixsen, D. J., Dwek, E., Mather, J. C., Bennett, C. L., & Shafer, R. A. 1998, *ApJ*, 508, 123  
 Frayer, D. T., Armus, L., Scoville, N. Z., et al. 2003, *AJ*, 126, 73  
 Fu, H., Cooray, A., Feruglio, C., et al. 2013, *Nature*, 498, 338  
 Geach, J. E., Chapin, E. L., Coppin, K. E. K., et al. 2013, *MNRAS*, 432, 53  
 Gonzalez, A. H., Clowe, D., Bradač, M., et al. 2009, *ApJ*, 691, 525  
 Greve, T. R., Bertoldi, F., Smail, I., et al. 2005, *MNRAS*, 359, 1165  
 Grogin, N. A., Kocevski, D. D., Faber, S. M., et al. 2011, *ApJS*, 197, 35

- Hickox, R. C., Wardlow, J. L., Smail, I., et al. 2012, *MNRAS*, 421, 284
- Ho, P. T. P., Moran, J. M., & Lo, K. Y. 2004, *ApJ*, 616, L1
- Hodge, J. A., Carilli, C. L., Walter, F., et al. 2012, *ApJ*, 760, 11
- Hodge, J. A., Karim, A., Smail, I., et al. 2013, *ApJ*, 768, 91
- Holland, W. S., Robson, E. I., Gear, W. K., et al. 1999, *MNRAS*, 303, 659
- Holland, W. S., Bintley, D., Chapin, E. L., et al. 2013, *MNRAS*, 2513
- Hughes, D. H., Serjeant, S., Dunlop, J., et al. 1998, *Nature*, 394, 241
- Iverson, R. J., Greve, T. R., Smail, I., et al. 2002, *MNRAS*, 337, 1
- Iverson, R. J., Greve, T. R., Dunlop, J. S., et al. 2007, *MNRAS*, 380, 199
- Keenan, R. C., Trouille, L., Barger, A. J., Cowie, L. L., & Wang, W.-H. 2010, *ApJS*, 186, 94
- Kneib, J., Ellis, R. S., Smail, I., Couch, W. J., & Sharples, R. M. 1996, *ApJ*, 471, 643
- Kneib, J.-P., van der Werf, P. P., Kraiberg Knudsen, K., et al. 2004, *MNRAS*, 349, 1211
- Knudsen, K. K., Kneib, J.-P., Richard, J., Petitpas, G., & Egami, E. 2010, *ApJ*, 709, 210
- Knudsen, K. K., Neri, R., Kneib, J.-P., & van der Werf, P. P. 2009, *A&A*, 496, 45
- Knudsen, K. K., van der Werf, P. P., & Kneib, J. 2008, *MNRAS*, 384, 1611
- Laird, E. S., Nandra, K., Pope, A., & Scott, D. 2010, *MNRAS*, 401, 2763
- Larson, D., Dunkley, J., Hinshaw, G., et al. 2011, *ApJS*, 192, 16
- Le Floch, E., Papovich, C., Dole, H., et al. 2005, *ApJ*, 632, 169
- Lilly, S. J., Eales, S. A., Gear, W. K. P., et al. 1999, *ApJ*, 518, 641
- Limousin, M., Richard, J., Jullo, E., et al. 2007, *ApJ*, 668, 643
- Magnelli, B., Elbaz, D., Chary, R. R., et al. 2009, *A&A*, 496, 57
- Magnelli, B., Lutz, D., Santini, P., et al. 2012, *A&A*, 539, A155
- Metcalf, L., Kneib, J.-P., McBreen, B., et al. 2003, *A&A*, 407, 791
- Michalowski, M. J., Dunlop, J. S., Cirasuolo, M., et al. 2012, *A&A*, 541, A85
- Miller, N. A., Fomalont, E. B., Kellermann, K. I., et al. 2008, *ApJS*, 179, 114
- Pello, R., Sanahuja, B., Le Borgne, J.-F., Soucail, G., & Mellier, Y. 1991, *ApJ*, 366, 405
- Quadri, R., Marchesini, D., van Dokkum, P., et al. 2007, *AJ*, 134, 1103
- Reddy, N. A., Erb, D. K., Pettini, M., Steidel, C. C., & Shapley, A. E. 2010, *ApJ*, 712, 1070
- Richard, J., Kneib, J.-P., Limousin, M., Edge, A., & Jullo, E. 2010a, *MNRAS*, 402, L44
- Richard, J., Smith, G. P., Kneib, J.-P., et al. 2010b, *MNRAS*, 404, 325
- Rieke, G. H., Young, E. T., Engelbracht, C. W., et al. 2004, *ApJS*, 154, 25
- Sault, R. J., Teuben, P. J., & Wright, M. C. H. 1995, in *Astronomical Society of the Pacific Conference Series*, Vol. 77, *Astronomical Data Analysis Software and Systems IV*, ed. R. A. Shaw, H. E. Payne, & J. J. E. Hayes, 433
- Scott, S. E., Dunlop, J. S., & Serjeant, S. 2006, *MNRAS*, 370, 1057
- Scott, S. E., Fox, M. J., Dunlop, J. S., et al. 2002, *MNRAS*, 331, 817
- Serjeant, S., Dunlop, J. S., Mann, R. G., et al. 2003, *MNRAS*, 344, 887
- Serjeant, S., Dye, S., Mortier, A., et al. 2008, *MNRAS*, 386, 1907
- Simpson, J., Swinbank, M., Smail, I., et al. 2014, *ApJ* submitted, arXiv:1310.6363
- Smail, I., Iverson, R. J., & Blain, A. W. 1997, *ApJ*, 490, L5
- Smail, I., Iverson, R. J., Blain, A. W., & Kneib, J. 2002, *MNRAS*, 331, 495
- Swinbank, M., Simpson, J., Smail, I., et al. 2014, *MNRAS* in press, arXiv:1310.6362
- Symeonidis, M., Georgakakis, A., Seymour, N., et al. 2011, *MNRAS*, 417, 2239
- Tacconi, L. J., Genzel, R., Smail, I., et al. 2008, *ApJ*, 680, 246
- Walter, F., Decarli, R., Carilli, C., et al. 2012, *Nature*, 486, 233
- Wang, S. X., Brandt, W. N., Luo, B., et al. 2013, *ApJ*, 778, 179
- Wang, W., Cowie, L. L., & Barger, A. J. 2004, *ApJ*, 613, 655
- . 2006, *ApJ*, 647, 74
- Wardlow, J. L., Smail, I., Coppin, K. E. K., et al. 2011, *MNRAS*, 415, 1479
- Webb, T. M., Eales, S. A., Lilly, S. J., et al. 2003, *ApJ*, 587, 41
- Weiß, A., Kovács, A., Coppin, K., et al. 2009, *ApJ*, 707, 1201
- Wold, I. G. B., Owen, F. N., Wang, W.-H., Barger, A. J., & Keenan, R. C. 2012, *ApJS*, 202, 2
- Younger, J. D., Fazio, G. G., Huang, J.-S., et al. 2009, *ApJ*, 704, 803
- Zemcov, M., Blain, A., Halpern, M., & Levenson, L. 2010, *ApJ*, 721, 424